photonics

Article

Simulation Study on 3D Heterogeneous Photonic Integration with Vertical Microring Coupler

Jiachen Liu [1,2], Yingying Zeng [1,2], Haifeng Hu [1,2], Ni Zhang [1,2], Qiwen Zhan [1,2] and Xiaogang Chen [1,3,*]

1 School of Optical-Electrical and Computer Engineering, University of Shanghai for Science and Technology, Shanghai 200093, China; liujiachen@usst.edu.cn (J.L.); 232200400@st.usst.edu.cn (Y.Z.); hfhu@usst.edu.cn (H.H.); zhangn@usst.edu.cn (N.Z.); qwzhan@usst.edu.cn (Q.Z.)
2 Zhangjiang Laboratory, 100 Haike Road, Shanghai 201204, China
3 Crealights Technology Co., Ltd., Suzhou 215155, China
* Correspondence: xiaogang.chen@crealights.com; Tel.: +86-0512-65920690

Abstract: We present a simulation-based study on a 3D heterogeneous photonic integration scheme based on a vertical microring coupler (VμRC). Our research introduces a more compact and efficient layout of photonic devices in the vertical direction, surpassing the limitations of traditional planar integration methods. This investigation focuses on optimizing the performance of the VμRC by analyzing critical parameters such as the dimensions of the microring and the waveguide and the refractive indices of surrounding materials, which serve as the guideline for future manufacturing of the device. The simulation results demonstrate that the careful selection and optimization of these parameters significantly impact the transmittance and coupling characteristics of the VμRC. To demonstrate the validity of this simulation model, we applied it to a few practical cases and achieved comparable results with our previous experiments.

Keywords: heterogeneous photonic integration; 3D heterogeneous integration; vertical microring coupler

check for updates

Citation: Liu, J.; Zeng, Y.; Hu, H.; Zhang, N.; Zhan, Q.; Chen, X. Simulation Study on 3D Heterogeneous Photonic Integration with Vertical Microring Coupler. *Photonics* **2024**, *11*, 251. https://doi.org/10.3390/photonics11030251

Received: 31 January 2024
Revised: 22 February 2024
Accepted: 7 March 2024
Published: 11 March 2024

1. Introduction

The rapid development of photonics has revolutionized various fields, including optical communication, sensing, and high-performance computing [1,2]. To meet the growing demand for compact and energy-efficient photonic devices, researchers have been exploring innovative integration methods, especially regarding integrating light sources onto silicon photonic chips. Previously reported solutions can be broadly divided into two categories: flip-chip bonding technology [3–5] and the direct growth of compound semiconductor lasers on silicon wafers [6,7]. However, both of these approaches necessitate direct contact between different material platforms. Due to inherent disparities in lattice constants, dielectric characteristics, thermal sensitivity, and fabrication processes, along with other intrinsic factors between these materials, significant limitations exist for integrating semiconductor lasers onto silicon wafers. In addition, photonic wire bonding is a process used in the manufacturing of optoelectronic devices [8,9]. However, photonic wire bonding is often associated with high production costs, potential throughput limitations, varying mechanical strength, and reliability concerns over time. Consequently, these limitations impede the achievable performance metrics of the overall photonic integrated chip. Three-dimensional (3D) photonic integration has emerged as a promising approach that enables the integration of multiple photonic components in a vertical stack, offering enhanced functionality and a reduced footprint [10–13]. Self-rolled-up micro-resonators monolithically integrated on a silicon ridge waveguide have been demonstrated as a viable route for realizing 3D photonic integration [14–18]. These vertical resonator structures can be easily fabricated using traditional planar processing technology [17,18], making them favorable candidates for building 3D photonic integrated circuits (PICs) utilizing matured semiconductor infrastructures [19]. The VμRC provides a compact and efficient means of coupling light between different photonic circuit device planes. By exploiting the evanescent field coupling mechanism, the VμRC enables the transmission of light signals with minimal loss and high coupling efficiency [20–22]. Compared to other methods such as wafer bonding, transfer printing, or other 3D heterogeneous photonic integration schemes, the proposed scheme of using vertical microring couplers for 3D photonic integration offers significant advantages in terms of reducing fabrication complexity, improving thermal management, and enhancing device functionality. It stands out for its compatibility with existing CMOS processes, scalability, and potential for high-density integration, positioning it as a promising solution for future photonic systems.

In previous work, we proposed a 3D heterogeneous photonic integration scheme that employed monolithically integrated SiN_x vertical microring couplers (VμRCs) on a silicon photonic ridge waveguide for interlayer coupling [15,17,18]. This integration scheme enabled the silicon photonic layer to access the active functionalities best suited to be implemented in the compound semiconductor material platform. Additionally, an efficient axial confinement approach was introduced, resulting in a vertical microring coupler that exhibited increased resonant mode spacing and single-mode operation in the telecommunication C-band and S-band [17]. However, these investigations focused on the coupling of microrings to the bottom silicon photonic waveguides. In comparison, we have extensively investigated InP semiconductor lasers; successfully demonstrated lasing in a hybrid square–rectangular laser configuration; analyzed the noise properties of the laser; and explored its potential applications in optical computing, optical logic, and various other application domains [23]. Research on transmitting optical signals from the active photonic device plane to the vertical microring and then coupling the microring to the passive silicon photonic device layer has not yet been carried out and is the focus of this article.

In order to further optimize performance and provide guidance for manufacturing high-performance and compact photonic devices, it is necessary to first conduct simulation-based research on the heterogeneously integrated 3D photonic system using the VμRC as the inter-layer coupling device. This research focuses on analyzing critical parameters, such as microring and waveguide dimensions, as well as the refractive index of surrounding materials. Through rigorous simulations, the optimal values for these parameters can be determined, leading to the improved coupling efficiency and transmission characteristics of the VμRC. Furthermore, this study investigates the transmission spectra of the VμRC at different ports, highlighting the field distributions of the resonant peaks within specific telecommunications bands. This analysis provides insights into the operating wavelengths and bandwidths of the VμRC, essential for designing efficient photonic devices for wavelength division multiplexing (WDM) in optical communication and sensing systems. The outcomes of this research not only contribute to the optimization of the VμRC but also provide guidance for the manufacturing of such a 3D heterogeneously integrated photonic system.

The proposed integration scheme does not require significant modification to either the silicon or the compound semiconductor-based fabrication process for the photonic integrated circuit system, resulting in minimum interruption to the existing infrastructure. By exploring the innovative 3D photonic integration method based on the VμRC, this study aims to advance the development of compact and high-performance photonic devices, enabling significant progress in inter-chip optical communication and self-sufficient photonic integrated systems.

2. Description of the Vertical Microring Coupler

A monolithically integrated VμRC on top of a passive silicon waveguide [15–18] offers great potential for further integrating active photonic integrated circuits (PICs) three-dimensionally to form a self-sufficient photonic system. We may envision that this advanced packaging scheme involves the codesigning of an active and passive PIC, monolithically placing the VμRC on the passive PIC, and fabricating a supporting structure on the active PIC device using selective area growth (SAG) with accurate-height, lithographically defined alignment trenches on the passive PIC device. After these two PICs are successfully and separately fabricated, we may use advanced alignment and packaging technics to form a self-sufficient photonic integrated system.

As illustrated in Figure 1, the proposed 3D heterogeneously integrated photonic system consists of an InP integrated chip and a silicon photonics chip. The VμRC formed by a self-rolled-up tube made of a strained SiN_x bilayer serves as the resonator coupler between these two photonic device planes. The InP device plane may host all active components such as lasers or modulators, while the silicon photonics device plane contains passive elements like waveguides, couplers, and switches. The detailed fabrication process of monolithically integrating the VμRC on top of the silicon photonic device plane can be found in our previous publications [15,17,18]. As discussed in reference [17], a thin layer (~21nm) of α-Si stripe can be deposited in the inner rim of the VμRC to raise the local effective index and therefore provide further optical confinement to the resonantly coupled field along the rolling axis and form a vertical microring instead of a microtube. This thin layer of α-Si contributes significantly to the resonant characteristics of the proposed 3D photonic system.

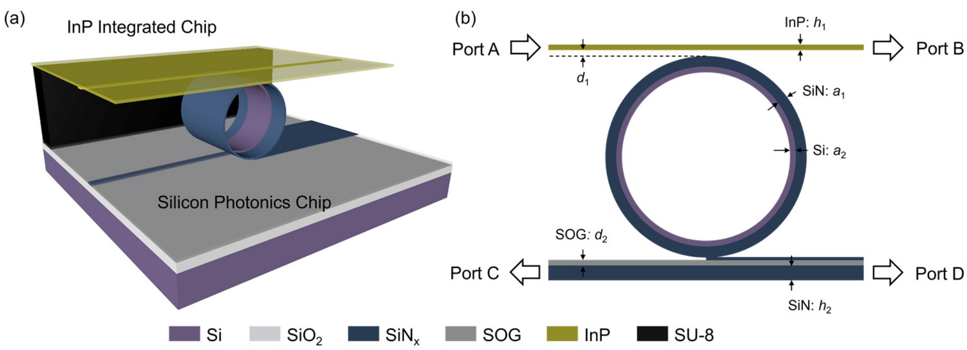

Figure 1. (**a**) The 3D and (**b**) 2D schematic diagrams of the vertical microring coupler.

In order to achieve precise alignment between the micro ring coupler and the InP chip, we may add a series of lithographically defined and placed mechanical support structures between the two layers of PIC chips, which involves the co-design of the silicon photonic layer and InP layer. Those supporting structures serve three functions at the same time. Firstly, they provide mechanical support to the two heterogeneous photonic device planes and the VµRC coupler in between to provide long-term mechanical stability to the 3D integrated device. Secondly, the co-design process ensures that those supporting structures and corresponding anchor sites are precisely placed on both chips to an accuracy provided by lithography which may serve as the alignment markers for device integration. Thirdly, the height of the supporting structures can be precisely controlled in the device growth stage using selective area growth (SAG) and therefore can help to maintain the designed coupling distance between the VμRC couplers and the two PIC device layers [24].

3. Simulation Results

3.1. The Coupling Process from the InP Waveguide to the Microring

The 3D vertical microring coupler, presented in Figure 1b, is structurally similar to a typical add-drop coupler configuration on a 2D plane involving one ring and two bus waveguides. Because of the self-rolled-up process of the SiN_x bilayer, the resulting 3D structure can be more precisely described as a spiral with all layers attached together. This structure can be approximated by a circular ring as long as the total thickness of the spiral structure is much less than its diameter [14], $N_t s \ll D_0$, where N_t is the winding number of the self-rolled-up tube, s is the thickness of the original bilayer SiN_x membrane, and D_0 is the diameter of the VμRC. This condition is satisfied for all the parameters chosen in the following simulations. This simplification allows for easier modeling and characterization of the device's optical properties, such as its resonant modes and coupling behavior. In this add-drop coupler configuration, assuming light is injected into the device through Port A using an integrated InP laser, it may subsequently be coupled from Port C to the silicon photonics circuitry via the VμRC.

For the study of the above model, we use the two-dimensional Wave Optics module in the commercial COMSOL Multiphysics simulation software based on the finite element method for analysis and research (https://www.comsol.jp/). Among the indices, the effective refractive indices of *a*-Si, SiN_x, SOG (Spin-on-Glass), and InP are 2.44, 1.9, 1.5, and 3.2, respectively, which are all obtained from measurements taken in previous experiments [17]. The inner diameter of the microring is taken to be 6.5 µm in accordance with the experimental results presented in [15,17,18], which can be adjusted by the differential stress within the SiN_x bilayer. The spectral position of the coupling wavelength is controlled by the structural parameters of the VμRC. In Figure 2a, we present the transmission spectra of three VμRCs, whose sidewall thickness a_1 = 350, 370, and 390 nm. One may notice that when a_1 is 370 nm, the two resonant peaks of the VμRC align precisely within the communication range of the S-band and C-Band, and the FSR of the VμRC is determined to be 52 nm, which matches very well with our previous experimental observation [17]. Using the same model, we calculated the transmission spectra of a series of VμRCs with different total thicknesses of the SiN_x layer, a_1, shown in Figure 2b. This result is consistent with what we observed experimentally [18].

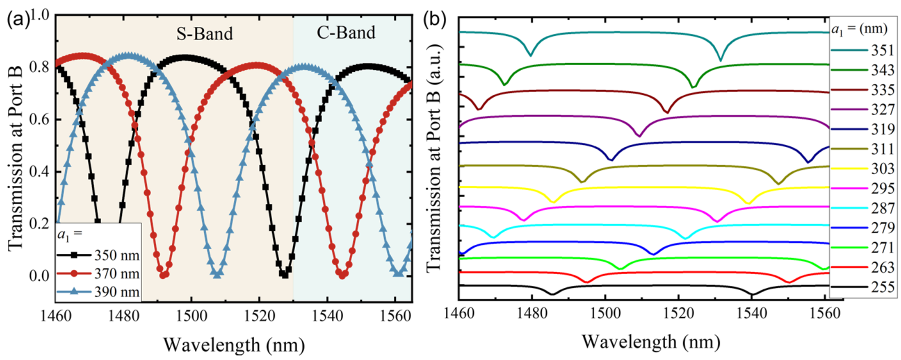

Figure 2. (**a**) Transmission of VμRC at Port B when a_1 = 350, 370, and 390 nm; (**b**) demonstration of the resonant wavelength passive tuning by varying the thickness of the SiN_x bilayer.

It is widely recognized that the free spectral region (FSR) of a microring cavity primarily depends on factors such as wavelength, group refractive index, and microring radius. This relationship can be expressed as follows [25]:

$$FSR = \frac{\lambda^2}{n_g \cdot L}$$

where n_g is the group refractive index and L is the length of the microcavity. In the case of a 3D inter-chip photonic coupling system using the wavelength division multiplexing (WDM) scheme, it is preferrable that the resonant coupling wavelength for each VμRC can be easily distinguished to avoid extra coupling noise from the adjacent channel. Thus, a larger FSR of the VμRC's resonant peaks is desired. As shown in Figure 2a, as the effective diameter decreases, the radiation loss increases, which causes the peaks to become broader and shallower [18]. This relationship is validated in our simulations, as shown in Figure 2b. It is evident that reducing the thickness of SiN_x thin films and decreasing the effective diameter leads to an increase in the 3 dB bandwidth of the coupling peak and a decrease in its peak intensity.

We have demonstrated experimentally that depositing a high-refractive-index thin silicon layer on the inner side of the silicon nitride microring results in increased axial confinement. The high-index strip within the microtube increases the effective refractive index locally. Therefore, the refractive index profile along the axial direction exhibits discontinuity similar to a step-index waveguide, which will help to confine the electromagnetic field within the high-refractive-index region and effectively form a vertical microring instead of a tube. In our previous experiment, we successfully achieved this by depositing a 21 nm *a*-Si thin film inside a VμRC [17] and observed a greatly increased FSR. However, the thickness of this silicon layer (a_2) also affects the radius of the VμRC, which, in turn, is related to the transmittance of the device. Therefore, in this study, we vary the thickness of the *a*-Si layer around the experimentally obtained value and demonstrate the impact of a_2 on the transmission of the VμRC at Port B when a_1 is set to 370 nm, as shown in Figure 3. An increase in the thickness of the silicon layer results in a slight redshift of the coupling peak of the VμRC. Based on the simulations, we identify a_2 = 25 nm as the optimal parameter for the next phase of our research. This value results in an increased effective diameter of the microring, leading to a transmission spectrum with the deepest and narrowest coupling peak. However, it is important to consider the self-rolled-up phenomenon caused by the internal stress difference in the silicon nitride bilayer. If the *a*-Si layer becomes excessively thick, it can pose challenges in terms of curling. Therefore, selecting a_2 = 25 nm is a suitable choice, striking a balance between achieving the desired transmission spectrum characteristics and avoiding difficulties associated with curling caused by excessive thickness.

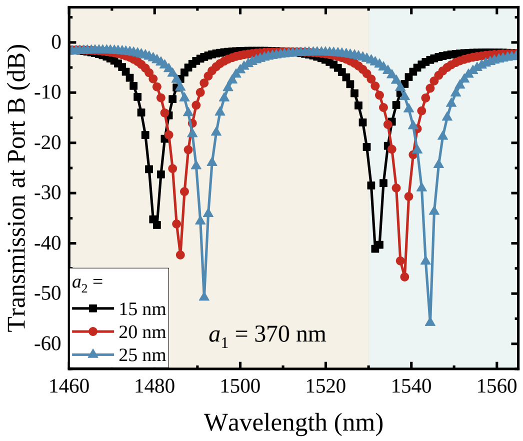

Figure 3. Transmission of VμRC at Port B as the thickness of the $a-$Si layer (a_2) varies.

In the two-dimensional VμRC model depicted in Figure 1b, the thickness of the upper InP waveguide (h_1) plays a significant role in determining the coupling coefficient (k_1) between the InP waveguide and the microring. This, in turn, affects the transmission at Ports B and C. Figure 4a illustrates the relationship between the transmission at Port B and the thickness of the InP waveguide. When h_1 is set to 80 nm, clear resonant dips in the transmission spectrum at Port B are observed at 1491.5 nm and 1544.4 nm with the smallest 3 dB bandwidth. To analyze the coupling coefficient k_1 between the InP waveguide and the VμRC in this scenario, we establish a model as presented in Figure 4c. The results of the coupling coefficient k_1 at different values of h_1 are obtained and depicted in Figure 4b. For the optimal coefficient h_1 = 80 nm obtained in Figure 4a, k_1 at 1491.5 nm and 1544.4 nm are 0.46 and 0.5, respectively, and the electric field distribution at the wavelength of 1544.4 nm is presented in Figure 4c. To calculate the coupling coefficient k_1, we select a half-ring waveguide configuration to inhibit light from resonating within the ring resonator. In modeling this setup, the structure is fully enclosed by Perfectly Matched Layers (PMLs) to eliminate reflections, with both ends of the half-ring waveguide directly interfacing with the PMLs. This arrangement ensures efficient coupling from Port 1 to Port 2 across the waveguide and the circular ring while effectively preventing light reflection at the waveguide's ports. Due to the higher polarization efficiency of TE mode for microtubes, TE-polarized light is used in the model.

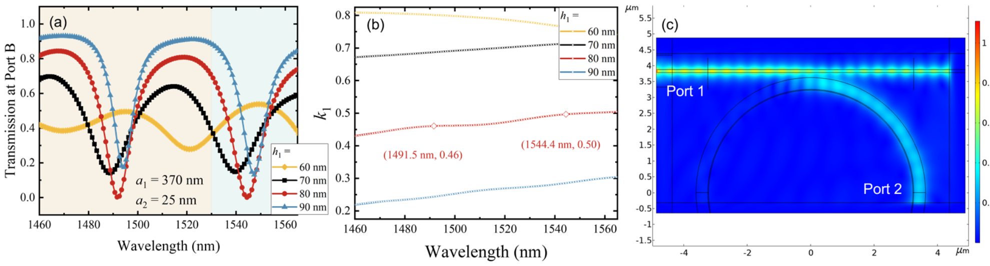

Figure 4. (**a**) Transmission at Port B and (**b**) coupling coefficient k_1 of VμRC at h_1 = 60, 70, 80, and 90 nm when a_1 = 370 and a_2 = 25 nm. (**c**) Electric field distribution at the wavelength of 1544.4 nm.

Apart from the thickness of the InP waveguide, the coupling distance between the InP waveguide and the microring also plays a pivotal role in determining the transmission spectrum. To investigate this, we vary the coupling distance (d_1) between the InP waveguide and the VμRC while keeping a_1 = 370, a_2 = 25, and h_1 = 80 nm constant. As shown in Figure 5a,b, the transmission at Port B and the corresponding coupling coefficient k_1 of VμRC are simulated and plotted for different d_1 values. Notably, as the coupling distance increases, the entire transmission spectrum of Port B redshifts, and the coupling coefficient k_1 exhibits a trend of first increasing and then decreasing. The maximum coupling coefficient between the InP waveguide and the microcavity is found at d_1 = 160 nm. Specifically, when d_1 = 160 nm, the coupling coefficients at the peak wavelengths of 1491.57 and 1544.4 nm was 0.46 and 0.5, respectively. Collectively, these results suggest that for the coupling process from the InP waveguide to the microring, the optimal parameters are a thickness of 370 nm for the SiN_x layer, 25 nm for the silicon layer, and 80 nm for the upper InP waveguide and a coupling distance of 160 nm. Under these conditions, we can obtain the highest coupling efficiency from the InP waveguide to the VμRC.

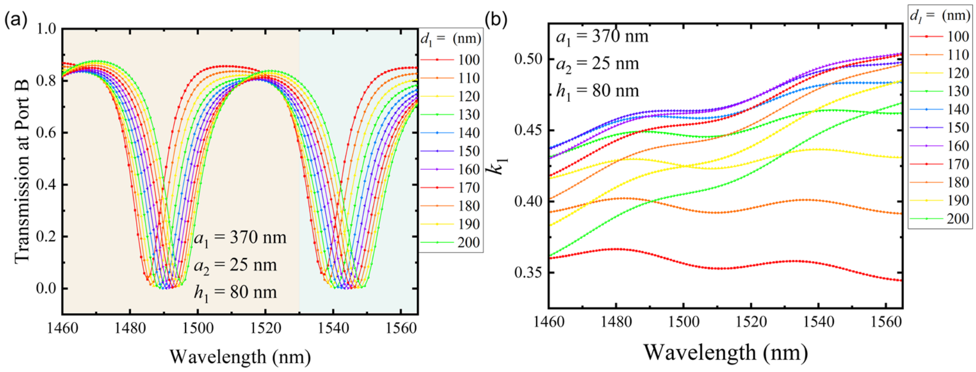

Figure 5. (**a**) Transmission at Port B and (**b**) coupling coefficient k_1 of VμRC at d_1 = 100 to 200 nm when a_1 = 370, a_2 = 25, and h_1 = 80 nm.

3.2. The Coupling Process from the Microring to the SiN_x Waveguide

In the aforementioned findings, we have successfully identified the optimal parameters for the coupling process from the InP waveguide to the VμRC. Indeed, the thickness of the silicon nitride waveguide (h_2) also plays a crucial role in determining the transmission spectrum of Port C, as depicted in Figure 1. By varying the thickness of h_2 within the range of 400 to 500 nm, we can observe changes in the resonance peak of the transmission spectrum. Figure 6a displays the simulated transmission spectrum at Port C for different h_2 values. As the thickness of h_2 increases, the resonance peak of the transmission spectrum redshifts. In this case, the maximum peak is observed at h_2 = 450 nm, indicating that this thickness provides the most favorable conditions for achieving the desired transmission characteristics. This parameter differs from the parameters used in previous experiments, providing guidance for future device optimization. The impact of h_2 on the VμRC device's performance is further illustrated by the corresponding coupling coefficient (k_2) diagram shown in Figure 6b. The choice of h_2 significantly affects the coupling coefficient and, consequently, the performance of the VμRC device.

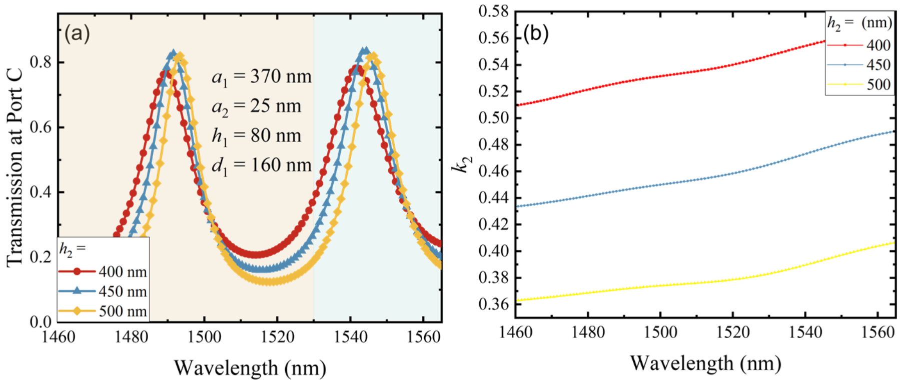

Figure 6. (**a**) Transmission at Port C and (**b**) coupling coefficient k_2 of VμRC at h_2 = 400, 450, and 500 nm when a_1 = 370, a_2 = 25, h_1 = 80, and d_1 = 160 nm.

In order to facilitate the self-rolling process and the formation of the VμRC on top of the silicon ridge waveguide, a layer of Spin-on-Glass (SOG) is applied on top of the silicon waveguide and then etched with RIE for planarization. The residual thickness of this SOG layer can be precisely controlled by the etching process. The thickness of this SOG layer, represented as d_2, assumes an important role in determining the overall coupling distance, thereby influencing the coupling coefficient between the VμRC and the underlying silicon waveguide. To comprehensively explore the effects of varying SOG thicknesses on the transmittance of the C-port, transmission spectra are simulated for SOG thicknesses of 30, 50, and 70 nm, as illustrated in Figure 7a. Notably, the maximum Port C transmittance is observed at a SOG thickness of 50 nm, which corresponds to coupling coefficients of 0.45 and 0.48 at wavelengths of 1491.57 nm and 1544.4 nm, respectively (see Figure 7b). The electric field distribution at the peak wavelength of 1544.4 nm is depicted in Figure 7c. These findings underscore the critical role of the SOG thickness in determining the performance of VμRCs.

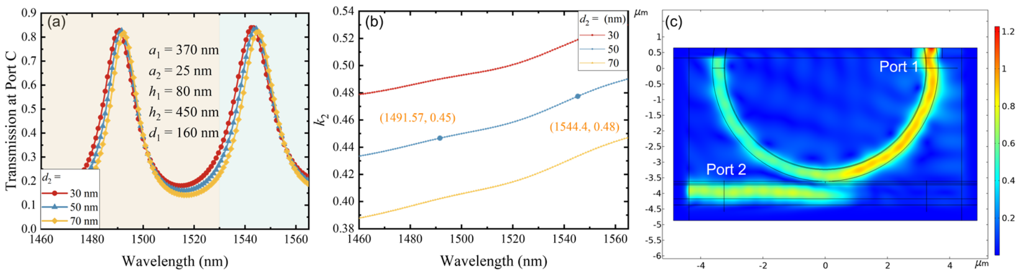

Figure 7. (**a**) Transmission at Port C and (**b**) coupling coefficient k_2 of VμRC at d_2 = 30, 50, and 70 nm when a_1 = 370, a_2 = 25, h_1 = 80, h_2 = 450, and d_1 = 160 nm. (**c**) Electric field distribution at the wavelength of 1544.4 nm.

Moreover, the investigation delves into the impact of the refractive index of the SOG material, denoted as n_{SOG}, on the transmittance of Port C, as visually depicted in Figure 8a. The variation in the refractive index of SOG exhibits negligible effects on the transmission spectrum. Subsequently, we conduct a comparative analysis between the transmission spectrum of the VμRC and its quality factor under the following dimensional parameters: a_1 = 370, a_2 = 25, h_1 = 80, h_2 = 450, d_1 = 160, and d_2 = 50 nm. Remarkably, the coupling peak between the two components aligns notably well with the highest $Q-$factor, thereby indicating a substantial correlation. The strategic application of high-index silicon layers and precision fabrication techniques significantly minimizes the impact of lateral photon leakage and surface roughness on the microcavity's quality factor. Moreover, by examining the transmittance spectrum of the drop port in Figure 8b, crucial information regarding the insertion losses of the VμRC at S−band and C−band can be obtained. The insertion losses are determined to be −1.58 dB and −1.48 dB, respectively, while the corresponding 3 dB bandwidths are calculated to be 9.6 nm and 11.32 nm, respectively. Overall, these results contribute to a comprehensive understanding of the VμRC's performance characteristics.

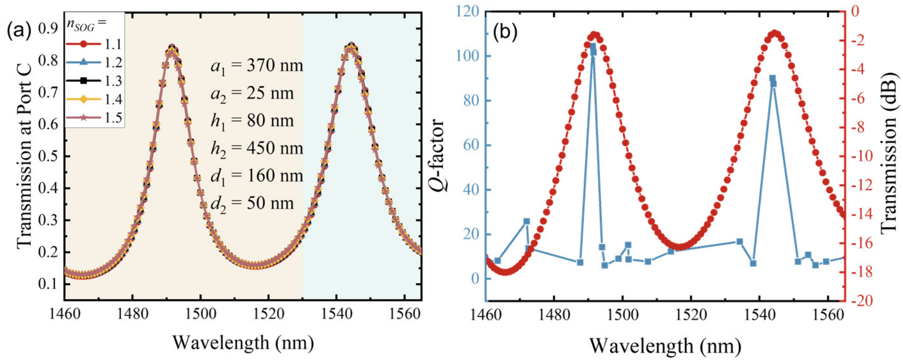

Figure 8. (**a**) Transmission at Port C of VμRC at n_{SOG} = 1.1, 1.2, 1.3, 1.4, and 1.5 when a_1 = 370, a_2 = 25, h_1 = 80, h_2 = 450, d_1 = 160, and d_2 = 50 nm. (**b**) Q-factor and transmission of the VμRC.

Subsequently, drawing upon the comprehensive set of simulation outcomes, successfully obtain the transmission spectra of the VμRC at Ports B, C, and D, as exemplified in Figure 9a. Notably, these spectra are acquired under the following dimensional parameters: a_1 = 370, a_2 = 25, h_1 = 80, h_2 = 450, d_1 = 160, and d_2 = 50 nm. Regarding the parameters a_1 and a_2, which denote the thicknesses of silicon nitride (SiN_x) and amorphous silicon (a−Si), respectively, we observe that these parameters critically influence the effective diameter of the annular cavity. Consequently, increases in a_1 and a_2 lead to the resonances becoming more narrowly defined and deeper. The dimensions of h_1, h_2, d_1, and d_2 are found to significantly impact the coupling coefficient, thereby affecting the coupling efficiency directly. Our analysis aims to identify their optimal values to enhance system performance. We also note that variations in the refractive index of the Spin−On−Glass (n_{SOG}) exhibit negligible impact on the transmission spectrum, aligning with our simulation results. Additionally, the electric field distributions of the coupling peaks from 1460nm to 1565 nm are depicted in Figure 9b,c, respectively. For the VμRC under investigation, the coupling wavelengths are determined to be 1491.57 and 1544.4 nm, respectively. As we proceed towards the subsequent stages of actual device fabrication, it is crucial to acknowledge that the VμRC is a three-dimensional entity. The comparison between the simulation results and the optimal parameters obtained in previous experiments [15,17,18] shows that the values of parameters a_1, a_2, and d_2 are consistent. As for h_2, a large waveguide thickness helps to enhance the coupling between the microring and the waveguide; improvements need to be made in future experiments.

In addition to the aforementioned parameters, the investigation of the VμRC along the axial direction of the cylinder assumes paramount importance. Building upon our previous research results, we identify the key parameters along the axial direction, namely a waveguide width of 2 µm and an a-Si strip width of 3 µm to correspond with it [17]. In fact, for actual three-dimensional microtubes, without the constraint of a−Si in the axial direction, the axial loss will be significant, and the VμRCs may support more than one axial mode. By considering both the radial and axial dimensions of the VμRC device, it is possible to achieve the precise control and optimization of its functionality, leading to improved performance and reliability in various photonic integrated circuit applications [17,18].

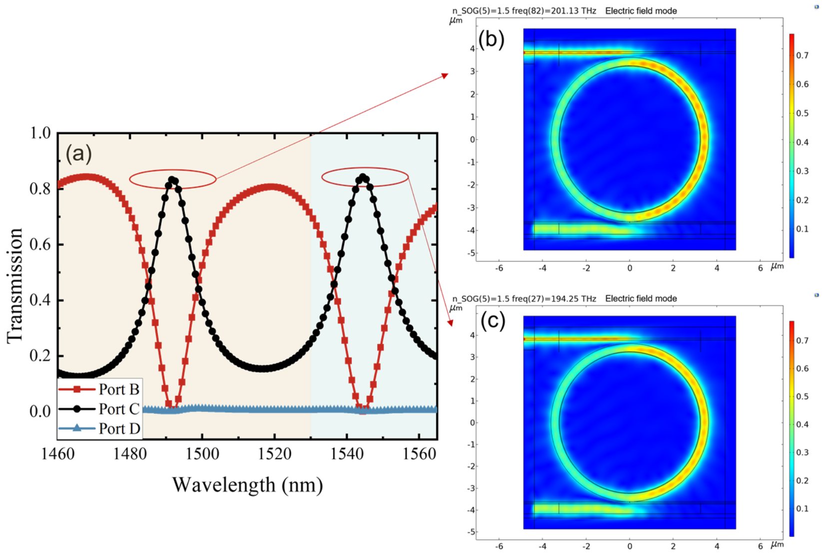

Figure 9. (**a**) Transmission at Port B, C, and D of VμRC when a_1 = 370, a_2 = 25, h_1 = 80, h_2 = 450, d_1 = 160, and d_2 = 50 nm. Electric field distribution at two coupling peaks with the wavelength of (**b**) 1491.57 and (**c**) 1544.4 nm.

The device under investigation is actually a 3D structure. A simplified 2D model may expedite the simulation process, but a true 3D simulation is the best way to verify the findings obtained using the 2D model. Subsequently, we perform such a 3D simulation using the following parameters: a_1 = 370, a_2 = 25, h_1 = 80, h_2 = 450, d_1 = 160, and d_2 = 50 nm, we set the thickness of all the waveguide in the z-direction to 2 µm, and we construct a three-dimensional model. The transmission spectrum and electromagnetic field results of the three-dimensional VμRCs' simulation are presented in Figure 10, which exhibit good consistency with the two-dimensional results shown in Figure 9. Furthermore, in Figure 10b, the electric field distribution in 3D of the resonant coupling peak at 1492 nm is elaborated. The efficacy of this structure in achieving optical coupling from the InP to SiN platform has been substantiated, thereby offering a novel approach for future heterogeneous photonics integration endeavors.

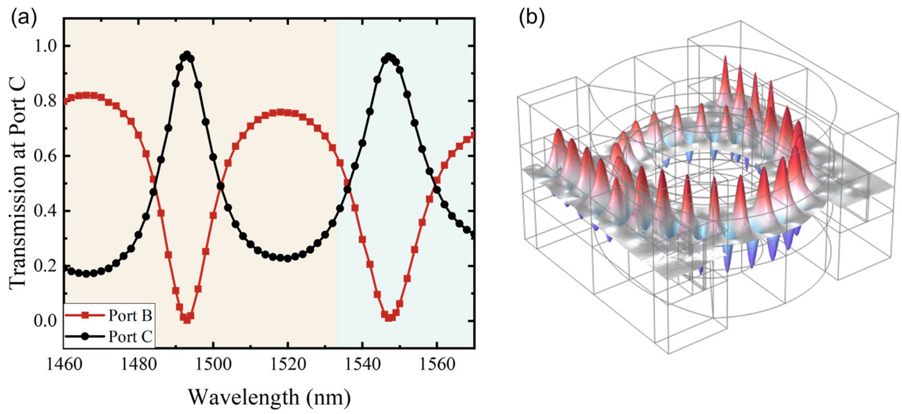

Figure 10. (**a**) Transmission at Port B and C of VμRC with 3D simulation when a_1 = 370, a_2 = 25, h_1 = 80, h_2 = 450, d_1 = 160, and d_2 = 50 nm. (**b**) Electric field distribution at the coupling peak with the wavelength of 1492 nm.

4. Conclusions

In conclusion, this paper investigates the structural and optical parameters for the performance analysis and optimization of the VμRC−based 3D heterogeneously photonic integrated circuits. By introducing a more compact and efficient vertical coupler between different photonic device planes, this method surpasses the limitations of traditional planar integration methods, offering enhanced performance and more versatile network topology. Through comprehensive simulations, various dimensional parameters, including waveguide widths, waveguide heights, and coupling distances, are determined for the VμRC. The obtained results highlight the crucial role of these parameters in governing the coupling efficiency and transmission characteristics of the VμRC. Notably, the optimal values of a_1 = 370, a_2 = 25, h_1 = 80, h_2 = 450, d_1 = 160, and d_2 = 50 nm are identified, providing invaluable guidance for the subsequent fabrication and optimization of the VμRCs. This study presents simulation-based transmission spectra of the VμRC at different ports, effectively demonstrating its single-mode operation within the telecom S-band and C-band, with insertion losses of -1.58 and -1.48 dB, and corresponding 3dB bandwidths of 9.6 and 11.32 nm. These findings establish a strong theoretical basis for achieving efficient optical transmission within specific telecommunication frequency bands. This research is committed to promoting the development of compact and high-performance photonic integrated devices, with the aim of opening up new avenues for the design and manufacturing of next-generation photonic systems and promoting breakthroughs in various fields that rely on efficient and reliable photonics.

Author Contributions: Conceptualization, X.C. and Q.Z.; methodology, J.L.; software, J.L., Y.Z., N.Z., and H.H.; validation, J.L.; formal analysis, J.L.; investigation, J.L.; resources, J.L.; data curation, J.L.; writing—original draft preparation, J.L.; writing—review and editing, X.C. and Q.Z.; visualization, J.L.; supervision, J.L.; project administration, J.L.; funding acquisition, X.C. and Q.Z. All authors have read and agreed to the published version of the manuscript.

Funding: This research was funded by National Natural Science Foundation of China, grant number 62275158 and 92050202.

Institutional Review Board Statement: Not applicable.

Informed Consent Statement: Not applicable.

Data Availability Statement: Data can be obtained from the corresponding author upon request.

Conflicts of Interest: Author Xiaogang Chen was employed by the company Crealights Technology Co., Ltd. The remaining authors declare that the research was conducted in the absence of any commercial or financial relationships that could be construed as a potential conflict of interest.

References

1. Marpaung, D.; Yao, J.; Capmany, J. Integrated microwave photonics. *Nat. Photonics* **2019**, *13*, 80–90. [CrossRef]
2. Wang, J.; Long, Y. On-chip silicon photonic signaling and processing: A review. *Sci. Bull.* **2018**, *63*, 1267–1310. [CrossRef]
3. Gösele, U.; Tong, Q.-Y. Semiconductor Wafer Bonding. *Annu. Rev. Mater. Sci.* **1998**, *28*, 215–241. [CrossRef]
4. Bao, S.; Wang, Y.; Lina, K.; Zhang, L.; Wang, B.; Sasangka, W.A.; Lee, K.E.K.; Chua, S.J.; Michel, J.; Fitzgerald, E.; et al. A review of silicon-based wafer bonding processes, an approach to realize the monolithic integration of Si-CMOS and III–V-on-Si wafers. *J. Semicond.* **2021**, *42*, 023106. [CrossRef]
5. Theurer, M.; Moehrle, M.; Sigmund, A.; Velthaus, K.-O.; Oldenbeuving, R.M.; Wevers, L.; Postma, F.M.; Mateman, R.; Schreuder, F.; Geskus, D.; et al. Flip-Chip Integration of InP to SiN Photonic Integrated Circuits. *J. Lightw. Technol.* **2020**, *38*, 2630–2636. [CrossRef]
6. Gasse, K.V.; Kerrebrouck, J.V.; Abbasi, A.; Verbist, J.; Torfs, G.; Moeneclaey, B.; Morthier, G.; Yin, X.; Bauwelinck, J.; Roelkens, G. III-V-on-Silicon Photonic Transceivers for Radio-Over-Fiber Links. *J. Lightw. Technol.* **2018**, *36*, 4438–4444. [CrossRef]
7. Hulme, J.C.; Shi, J.W.; Kennedy, M.J.; Komljenovic, T.; Szafraniec, B.; Baney, D.; Bowers, J.E. Fully integrated heterodyne microwave generation on heterogeneous silicon-III/V. In Proceedings of the 2016 IEEE International Topical Meeting on Microwave Photonics (MWP), Long Beach, CA, USA, 31 October–3 November 2016; pp. 336–339.
8. Lindenmann, N.; Balthasar, G.; Hillerkuss, D.; Schmogrow, R.; Jordan, M.; Leuthold, J.; Freude, W.; Koos, C. Photonic wire bonding: A novel concept for chip-scale interconnects. *Opt. Express* **2012**, *20*, 17667–17677. [CrossRef]
9. Billah, M.R.; Blaicher, M.; Hoose, T.; Dietrich, P.-I.; Marin-Palomo, P.; Lindenmann, N.; Nesic, A.; Hofmann, A.; Troppenz, U.; Moehrle, M.; et al. Hybrid integration of silicon photonics circuits and InP lasers by photonic wire bonding. *Optica* **2018**, *5*, 876–883. [CrossRef]
10. Yoo, S.J.B.; Guan, B.; Scott, R.P. Heterogeneous 2D/3D photonic integrated microsystems. *Microsyst. Nanoeng.* **2016**, *2*, 16030. [CrossRef]

11. Valligatla, S.; Wang, J.; Madani, A.; Naz, E.S.G.; Hao, Q.; Saggau, C.N.; Yin, Y.; Ma, L.; Schmidt, O.G. Selective Out-of-Plane Optical Coupling between Vertical and Planar Microrings in a 3D Configuration. *Adv. Opt. Mater.* **2020**, *8*, 2000782. [CrossRef]
12. Li, X. Self-rolled-up microtube ring resonators: A review of geometrical and resonant properties. *Adv. Opt. Photonics* **2011**, *3*, 366–387. [CrossRef]
13. Zhang, Z.; Felipe, D.; Katopodis, V.; Groumas, P.; Kouloumentas, C.; Avramopoulos, H.; Dupuy, J.-Y.; Konczykowska, A.; Dede, A.; Beretta, A.; et al. Hybrid Photonic Integration on a Polymer Platform. *Photonics* **2015**, *2*, 1005–1026. [CrossRef]
14. Chen, X. An analytical model to investigate the resonant modes of the self-rolled-up microtube using conformal transformation. *Opt. Express* **2014**, *22*, 16363–16376. [CrossRef] [PubMed]
15. Yu, X.; Arbabi, E.; Goddard, L.L.; Li, X.; Chen, X. Monolithically integrated self-rolled-up microtube-based vertical coupler for three-dimensional photonic integration. *Appl. Phys. Lett.* **2015**, *107*, 031102. [CrossRef]
16. Madani, A.; Kleinert, M.; Stolarek, D.; Zimmermann, L.; Ma, L.; Schmidt, O.G. Vertical optical ring resonators fully integrated with nanophotonic waveguides on silicon-on-insulator substrates. *Opt. Lett.* **2015**, *40*, 3826–3829. [CrossRef] [PubMed]
17. Yu, X.; Goddard, L.L.; Li, X.; Chen, X. Enhanced axial confinement in a monolithically integrated self-rolled-up SiNx vertical microring photonic coupler. *Appl. Phys. Lett.* **2016**, *109*, 111104. [CrossRef]
18. Yu, X.; Goddard, L.L.; Zhu, J.; Li, X.; Chen, X. Passive wavelength tuning and multichannel photonic coupling using monolithically integrated vertical microresonators on ridge waveguides. *Appl. Phys. Lett.* **2018**, *112*, 021108. [CrossRef]
19. Zhong, Q.; Tian, Z.; Veerasubramanian, V.; Dastjerdi, M.H.T.; Mi, Z.; Plant, D.V. Thermally controlled coupling of a rolled-up microtube integrated with a waveguide on a silicon electronic-photonic integrated circuit. *Opt. Lett.* **2014**, *39*, 2699–2702. [CrossRef]
20. Kipp, T.; Welsch, H.; Strelow, C.; Heyn, C.; Heitmann, D. Optical Modes in Semiconductor Microtube Ring Resonators. *Phys. Rev. Lett.* **2006**, *96*, 077403. [CrossRef]
21. Tian, Z.; Veerasubramanian, V.; Bianucci, P.; Mi, Z.; Kirk, A.G.; Plant, D.V. Selective polarization mode excitation in InGaAs/GaAs microtubes. *Opt. Lett.* **2011**, *36*, 3506–3508. [CrossRef]
22. Saggau, C.N.; Gabler, F.; Karnaushenko, D.D.; Karnaushenko, D.; Ma, L.; Schmidt, O.G. Wafer-Scale High-Quality Microtubular Devices Fabricated via Dry-Etching for Optical and Microelectronic Applications. *Adv. Mater.* **2020**, *32*, 2003252. [CrossRef] [PubMed]
23. Liu, J.C.; Huang, Y.Z.; Hao, Y.Z.; Fan, Y.R.; Wu, J.L.; Yang, K.; Xiao, J.L.; Yang, Y.D. Relative Intensity Noise and Linewidth for Hybrid-Cavity Semiconductor Lasers. *J. Lightw. Technol.* **2022**, *40*, 2087–2096. [CrossRef]
24. Kim, J.D.; Chen, X.; Coleman, J.J. 10-Selective Area Masked Growth (Nano to Micro). In *Handbook of Crystal Growth*, 2nd ed.; Kuech, T.F., Ed.; North-Holland: Boston, MA, USA, 2015; pp. 441–481.
25. Bogaerts, W.; De Heyn, P.; Van Vaerenbergh, T.; De Vos, K.; Kumar Selvaraja, S.; Claes, T.; Dumon, P.; Bienstman, P.; Van Thourhout, D.; Baets, R. Silicon microring resonators. *Laser Photon. Rev.* **2012**, *6*, 47–73. [CrossRef]